Oxygen isotope analysis of olivine by ion microprobe: matrix effects and applications to a serpentinised dunite

Maria Rosa Scicchitano[a*], Daniela Rubatto[a,b,c], Jörg Hermann[a,b], Alik S. Majumdar[d], Andrew Putnis[e]

[a] Research School of Earth Sciences, Australian National University, Canberra 2601 ACT, Australia (mari.scicchitano@anu.edu.au)

[b] Institute of Geological Sciences, University of Bern, 3012 Bern, Switzerland (daniela.rubatto@geo.unibe.ch; joerg.hermann@geo.unibe.ch)

[c] Institute of Earth Sciences, University of Lausanne, Geopolis, 1015 Lausanne, Switzerland

[d] Geosciences Division, Physical Research Laboratory, Navrangpura, Ahmedabad 380 009, Gujarat, India (asmajumdar@prl.res.in)

[e] The Institute for Geoscience Research, Curtin University, Perth 6845 WA, Australia (andrew.putnis@curtin.edu.au)

Corresponding author. E-mail: mari.scicchitano@anu.edu.au

Declarations of interest: none.

ABSTRACT

In order to resolve inter- and intracrystalline oxygen isotopic heterogeneities in olivine crystals encountered in mantle peridotites, basaltic lavas, chondritic meteorites and metamorphic rocks, *in situ* techniques such as ion microprobes are needed. Accurate ion microprobe analysis requires not only well-characterised reference materials, but also calibration of the matrix bias for compositional variations within a given mineral.

We investigated matrix bias effects related to Mg/Fe variations in olivine during *in situ* analysis of oxygen isotopes with sensitive high-resolution ion microprobe (SHRIMP) by analysing chemically homogenous olivine samples with forsterite contents in the range Fo_{74}–Fo_{100}. The isotopic measurements were calibrated against San Carlos olivine (SCO; Fo_{91}). The repeatability achieved for all samples was ± 0.21–0.50‰ (standard deviation, SD, at 95% confidence level, c.l.) comparable to that of San Carlos olivine (± 0.31–0.48‰, SD at 95% c.l.). A matrix bias up to ~ –2.0‰ was observed in olivine with forsterite content above 92 mole %, conversely to what has been reported for Cameca instruments. The relationship between the magnitude of matrix bias and fayalite content (mole %) is described by the quadratic function:

$$Bias_{Fa} = -0.0062\ Fa^2 + 0.233\ Fa - 1.60$$

The correction scheme for the matrix bias was applied to chemically zoned olivine crystals from a partly serpentinised dunite from the Archean Nuasahi massif (eastern India). Olivine cores (Fo_{92}) preserve their typical mantle-like signature with a $\delta^{18}O$ value of 5.16 ± 0.30‰ (σ at 95% c.l.). During a low temperature stage of serpentinisation, olivine transformed to $lizardite_1$+brucite+magnetite. Olivine rims (Fo_{98}; $\delta^{18}O$ = 1.92 ± 0.60‰, σ at 95% c.l.) and the surrounding $lizardite_2$ (4.87 ± 0.53‰, σ at 95% c.l.), formed during a later stage of rock-fluid interaction, are in isotopic equilibrium at ~ 405–430°C, with a fluid having a $\delta^{18}O$ of ~ 5.3–6.9‰. Evolved seawater enriched in ^{18}O by isotopic exchange during infiltration could have been responsible for this later serpentinisation stage observed in the Nuasahi massif. The concomitant analysis of oxygen isotopes at the microscale in both olivine and serpentine represents a powerful tool to constrain the nature and source(s) of serpentinising fluid(s) as well as the temperature of serpentinisation.

52 Keywords: oxygen isotopes, SHRIMP ion microprobes, olivine, matrix effects, Nuasahi massif,
53 serpentinized dunite
54

1. INTRODUCTION

Olivine is one of the major constituents of the Earth's mantle and meteorites as well as of some plutonic and volcanic igneous rocks. Oxygen isotope analysis of olivine from terrestrial and extra-terrestrial rocks has proven to be a powerful tool to identify interactions between different isotopic reservoirs during planetary formation and differentiation such as recycling of crustal material into the Earth's mantle, contamination of mantle magmas by assimilation of crustal material, and even interactions between chondritic melts and surrounding gas during chondrule formation (e.g., Deines and Haggerty, 2000; Zhang et al., 2000; Gurenko and Chaussidon, 2002; Bindeman et al., 2006, 2008; Chaussidon et al., 2008; Kita et al., 2010; Ushikubo et al., 2012; Tenner et al., 2013, 2015). Most of the oxygen isotopic compositions in olivine have been measured using bulk laser fluorination techniques on mineral concentrates. Studies of mantle peridotites, for instance, have demonstrated that the Earth's upper mantle is rather homogenous in its oxygen isotopic composition ($\delta^{18}O_{mantle}$ = 5.5‰, $\delta^{18}O_{olivine}$ = 5.18 ± 0.28‰; e.g., Mattey et al., 1994; Chazot et al., 1997). Nevertheless, other studies performed on some peridotitic xenoliths from kimberlites (e.g., Deines and Haggerty, 2000; Zhang et al., 2000) observed oxygen isotopic disequilibrium and intracrystalline isotopic heterogeneities interpreted as the result of mantle metasomatism. Additionally, light bulk oxygen isotopic compositions ($\delta^{18}O_{olivine}$ from 2.9 to 4.1‰) recently measured by Byerly et al. (2017) in olivine from Archean komatiites and interpreted as a primordial mantle heterogeneity, suggest that the Earth's mantle might be more heterogeneous than previously thought. Oxygen isotope analyses of single olivine crystals from basaltic lavas have also revealed significant oxygen

isotopic heterogeneities (e.g., $\delta^{18}O_{olivine}$ from 2.3 to 6.9‰ in basalts from Iceland; Gurenko and Chaussidon, 2002; Bindeman et al., 2006, 2008) compared to previous bulk analyses performed on mineral concentrates (e.g., Eiler, 2001), suggesting complex histories of magma generation, mixing and differentiation prior to eruption (e.g., Bindeman et al., 2006, 2008). These complexities are further validated by *in situ* oxygen isotope analyses by ion microprobe that highlighted intracrystalline oxygen isotope zoning up to 2.5‰ in single olivine phenocrysts from basaltic lavas in Iceland (Gurenko and Chaussidon, 2002).

Ion microprobe analysis is best suited to investigate oxygen isotopic heterogeneities at the microscale in olivine crystals from both terrestrial (e.g., mantle peridotites, basaltic lavas, serpentinites) and extraterrestrial rocks (e.g., chondritic meteorites; e.g., Chaussidon et al., 2008; Kita et al., 2010; Ushikubo et al., 2012; Tenner et al., 2013, 2015). In order to obtain accurate measurements by ion microprobe it is essential that the reference material has a chemical composition as close as possible to that of the sample, because of significant matrix bias effects related to variations in the chemical composition observed in some minerals (e.g., Eiler et al., 1997; Vielzeuf et al., 2005; Valley and Kita, 2009; Page et al., 2010; Rollion-Bard and Marin-Carbonne, 2011; Martin et al., 2014; Rubatto et al., 2014; Śliwiński et al., 2016). Previous studies with Cameca ion microprobes have, for instance, highlighted the occurrence of matrix bias effects as a function of Mg/Fe ratio in olivine during oxygen isotope analysis (e.g., Bindeman et al., 2008; Kita et al., 2010; Nakashima et al., 2013; Tenner et al., 2015; Isa et al., 2017).

In this study, we investigated matrix bias effects in olivine in the compositional range Fo_{74}–Fo_{100} during *in situ* analysis of oxygen isotopes with the SHRIMP ion microprobes. The developed matrix bias correction scheme is then applied to

chemically zoned olivine crystals (Fo_{92} cores and Fo_{98} rims) from a partly serpentinised dunite from the Nuasahi massif (eastern India) in order to constrain the source(s) of the serpentinising fluid(s) and the temperature of serpentinisation in this Archean peridotite. Further constraints on the serpentinisation process were obtained by oxygen isotope analysis at the microscale of lizardite surrounding the olivine crystals.

2. OLIVINE SAMPLES

The olivine crystals S3, SJ6 and P29 provided by Dr. Christoph Beier (GeoZentrum Nordbayern, Universität Erlangen-Nürnberg) and Dr. Felix Genske (Institut für Mineralogie, Westfälische Wilhelms-Universität Münster) were previously separated from lavas from the Azores Islands and characterised for their chemical and bulk oxygen isotopic compositions by Genske et al. (2013). The olivine crystals VS2A, VS18 and 6702-B1 provided by Dr. Peter Tollan (University of Bern) are from cumulate xenoliths from the Lesser Antilles Islands and were previously characterised for chemical and bulk oxygen isotopic compositions (Tollan, 2014; Tollan et al., 2012; 2017). The olivine JUB is a natural forsterite separated from a marble from the Ubehebe peak contact aureole (Roselle et al. 1999) provided by Prof. Lukas Baumgartner (University of Lausanne). Samples Fo_{99} (unknown provenance) and Fo_{93} (Pakistan) are natural Mg-rich olivine crystals of metamorphic origin, bought at a mineral fair and provided by Dr. Michael Jollands (University of Lausanne). Sample Fo_{100} is a synthetic forsterite grown by the Solix Corporation (Belarus) with the Czochralski method and was donated by Prof. Hugh O'Neill (Research School of Earth Sciences, ANU).

Analyses performed by EDXA-SEM or electron microprobe (see section 3.2.) indicate that all samples are chemically homogenous and their forsterite content (MgO/[MgO+FeO] on a molar basis, Mg#) spans over the range Fo_{74} to Fo_{100} (Table 1). Reference $\delta^{18}O$ values are reported in Table 2.

3. ANALYTICAL METHODS

3.1. Sample preparation

Seven olivine grains with different forsterite content were mounted in the central part of 25 mm epoxy mounts together with San Carlos olivine (SCO). The mounts were polished with a final 1 µm diamond paste to obtain flat analytical surfaces. Three olivine crystals (S3, SJ6, P29) were already mounted in the central part of an epoxy disc and could not be re-mounted together with the reference material for ion microprobe analyses. Small pieces of thin section from a partly serpentinised dunite belonging to the ultramafic complex of the Nuasahi Massif (eastern India) were mounted separately together with San Carlos olivine and antigorite Al06-44A (Scicchitano et al., 2018).

3.2. Major elements

The chemical homogeneity and zoning of the samples as well as the occurrence of inclusions and fractures was investigated by back-scattered electron imaging using the Jeol JSM-6610A SEM at the Research School of Earth Sciences (Australian National University, ANU). The instrument was operating at ~ 15 kV. Quantitative major

element analyses of olivine were obtained either with a Hitachi S-4300 SE/N FESEM scanning electron microscope equipped with an INCA X-MAX energy-dispersive X-ray analysis (EDXA) system at the Centre for Advanced Microscopy (ANU) (samples JUB, Fo_{100}, 6702-B1), or a Jeol JXA-8200 electron microprobe at the Institute of Geological Sciences (University of Bern) (samples Fo_{99}, Fo_{93}, VS2A, VS18, P29, SJ6, S3). Spot analyses were performed on four of the olivine samples for which there were no published chemical compositions (Fo_{100}, Fo_{99}, Fo_{93}, JUB) as well as to confirm the chemical compositions of the other olivine crystals (6702-B1, Table 2 in Tollan et al., 2017; VS2A and VS18, Supplementary Table 2 in Tollan et al., 2012; P29, SJ6 and S3, Supplementary Table DR1 in Genske et al., 2013). Analyses with the Hitachi-4300 SEM were performed using an accelerating voltage of 15 kV, a current of 0.6 nA, a working distance of 25 mm and a total acquisition time of 60 seconds. Synthetic standards (periclase, sanidine, marcasite, rutile, Cr_2O_3, and Ni) were used for the calibration. Electron microprobe analyses were conducted at an accelerating voltage of ~ 15 kV and current of ~ 20 nA. For each element, counting times were 20 seconds on background and 10 seconds on peak positions. Analyses were calibrated using the standards H081-anor81 (for Al_2O_3 and CaO), H003_albi3 (for Na_2O), H101_alm101 (for FeO), H015_fors15 (for SiO_2 and MgO), H044_teph44 (for MnO), and B14_buns14 (for NiO). Detection limits were 0.1 wt.% and 0.02 wt.% for SEM and EPMA analyses, respectively.

3.3. Oxygen isotope analysis by laser fluorination

A small fragment of three of the olivine samples (Fo_{100}, Fo_{99}, Fo_{93}) was crushed and ~ 20 mg of the 250–420 µm fraction was hand-picked in preparation for oxygen isotope

179 analyses by laser fluorination. The crystals were free of any inclusions being either
180 synthetic (Fo_{100}) or of gem-quality (Fo_{99} and Fo_{93}). Nevertheless, the mineral separates
181 were checked for purity using a binocular reflected light microscope.
182 All oxygen isotope data are expressed using the δ-notation relative to Vienna Standard
183 Mean Ocean Water (V-SMOW; Hoefs, 2009) with an $^{18}O/^{16}O$ ratio of 0.00200520
184 (Baertschi, 1976). Laser fluorination analyses of samples Fo_{99} and Fo_{93} were performed
185 at the Stable Isotope Laboratory of the University of Lausanne using a CO_2-laser
186 connected to a Finnigan MAT 253 mass spectrometer (e.g., Lacroix and Vennemann,
187 2015). Analyses were normalised to quartz NBS-28 ($\delta^{18}O$ = 9.64‰; Coplen et al.,
188 1983), which returned values of 9.62 ± 0.05‰ (1σ) over the analytical session. The
189 oxygen isotopic reference value for the synthetic pure forsterite (Fo_{100}) was obtained at
190 the University of Science and Technology of China in Hefei using a 25W MIR-10 CO_2-
191 laser connected to a Delta S mass spectrometer (e.g., Zha et al., 2010). Three reference
192 materials were used: UWG-2 garnet ($\delta^{18}O$ = 5.8‰; Valley et al., 1995), 04BXL07
193 garnet ($\delta^{18}O$ = 3.7‰; Gong et al., 2007), and SCO-1 olivine ($\delta^{18}O$ = 5.2‰; Eiler et al.,
194 1995). The repeatability of the measurements of each reference material on a given day
195 was better than ± 0.1‰ (1σ) for $\delta^{18}O$.
196 The oxygen isotopic reference value for sample 6702-B1 was provided by Dr. Peter
197 Tollan (University of Bern) and the analytical procedure is described in Tollan (2014).
198 The JUB olivine oxygen isotopic composition was provided by Prof. Lukas
199 Baumgartner and Dr. Benita Putlitz (University of Lausanne) and was measured at the
200 Stable Isotope Laboratory of the University of Lausanne following the analytical
201 protocol described in Lacroix and Vennemann (2015).
202

3.4. Oxygen isotope analysis by SHRIMP

Oxygen isotopic compositions of olivine at the microscale were determined with the SHRIMP II and SHRIMP SI ion microprobes at the Research School of Earth Sciences, ANU (Ireland et al., 2008) over a period of approximately two years, from November 2014 to September 2016. Matrix bias effects related to variations in the Mg/Fe ratio in olivine were investigated by referencing the analyses to San Carlos olivine (Mg# = 91 mole %) for which we assumed a $\delta^{18}O = 5.27 \pm 0.10‰$ encompassing all previously published oxygen isotope reference values (e.g., Eiler et al., 1995; 2000; Bindeman et al., 2008; Ahn et al., 2012; Isa et al., 2017).

The grain mounts were coated with aluminium or gold and stored in a vacuum oven at 60°C for at least 48 hours before being loaded into the SHRIMP. Analyses were performed using a 15 kV Cs^+ primary ion beam producing a primary beam current of ~ 4 nA. Each analytical spot was pre-sputtered for 60 to 120 seconds before the onset of analysis to allow for the stabilisation of the oxygen isotopic composition of the secondary ion beam (Ickert et al., 2008). Electrometer backgrounds were measured during pre-sputtering. EISIE (electron-induced secondary ion emission) was measured before and after each analysis. The analysed spot was ~ 25 × 20 µm in diameter during all analytical sessions. The $^{16}O^-$ and $^{18}O^-$ ions were measured in multicollection using Faraday cups with electrometers having 10^{10} Ω and 10^{11} Ω input resistors, respectively (Ickert et al., 2008). The mass resolution required for measuring $^{18}O/^{16}O$ is ~ 2300 (Ickert et al., 2008).

The reference material was analysed every three to five unknowns throughout the session. The mount with the olivine crystals S3, SJ6, and P29 was located in the sample chamber together with a second mount containing San Carlos olivine. This allowed a

regular analysis of the reference material by moving from one mount to the other. Typical count rates on $^{16}O^-$ and $^{18}O^-$ were 1.6–2.2 × 10^9 cps and 3.2–4.5 × 10^6 cps for olivine, 1.4–1.5 × 10^9 cps and 2.9–3.0 × 10^6 cps for serpentine (supplementary material, Tables S1–S4). Each analysis consisted of a total counting time of between 100 and 120 seconds, with sub measurements of 10 or 20 seconds each.

The in-house software POXI MC (P. Lanc) was used to apply background, EISIE, and potential drift corrections. Background corrections were done by using a mean, a polynomial or a Savitsky-Golay fitting for the whole session. Two analytical sessions out of four required correction for a linear drift (up to ~ 0.26‰ correction over the session), which was automatically applied by the in-house software POXI MC.

4. DATA TREATMENT

4.1. Estimation and correction of instrumental mass bias

SIMS analyses are affected by instrumental- and sample-related parameters known as "instrumental mass bias", including instrumental mass fractionation (IMF) and matrix bias (Huberty et al., 2010). IMF represents the variation in the oxygen isotopic ratios measured by ion microprobe compared to the true values induced by non-sample related parameters, such as differences in the efficiency of ionisation, transmission through the mass spectrometer and detection of individual isotopes (e.g., Shimizu and Hart, 1982; Eiler et al., 1997; Kita et al., 2009; Huberty et al., 2010; Page et al., 2010). IMF is described by a fractionation factor, $\alpha^{18}O_{SIMS}$ (e.g., Deloule et al., 1991; Eiler et al., 1997; Ickert et al., 2008; Kita et al., 2009; Martin et al., 2014):

$$\alpha^{18}O_{SIMS} = \frac{1 + (\delta^{18}O_{RAW(SCO\ or\ Al06\text{-}44A)} / 1000)}{1 + (\delta^{18}O_{LF(SCO\ or\ Al06\text{-}44A)} / 1000)} \quad (1)$$

Where $\delta^{18}O_{RAW}$ and $\delta^{18}O_{LF}$ are the oxygen isotopic ratios expressed on the V-SMOW scale measured in a given reference material by ion microprobe and laser fluorination, respectively. For the data reported in this study, $\alpha^{18}O_{SIMS}$ (Eq. 1) was established by measurements of San Carlos olivine (for olivine) and antigorite Al06-44A (for serpentine), which we used as the running standards (supplementary material, Tables S2 and S4). Antigorite Al06-44A was used because no lizardite reference material was available at the time. Oxygen isotope ratios measured in all other olivine and serpentine samples were then corrected for the corresponding IMF according to the following equation (e.g., Kita et al., 2009):

$$\delta^{18}O^{*} = \left\{ \frac{[1 + (\delta^{18}O_{RAW(olivine\ or\ serpentine)} / 1000)]}{\alpha^{18}O_{SIMS\ (SCO\ or\ Al06\text{-}44A)}} - 1 \right\} \times 1000 \quad (2)$$

Oxygen isotopic ratios corrected for IMF relative to a reference material are indicated in this study as $\delta^{18}O^{*}$ (supplementary material, Tables S1–S4). In the SHRIMP laboratory at the Research School of Earth Sciences, the IMF correction is automatically applied with the in-house software POXI MC on oxygen isotopic ratios previously corrected for background as well as EISIE and drift, if necessary (Ickert et al., 2008; Martin et al., 2014).

The matrix bias is defined as the remaining difference between the oxygen isotopic ratios corrected for IMF and the laser fluorination reference values for the other olivine reference materials with various chemical compositions (e.g., Kita et al., 2009; Page et al., 2010; Martin et al., 2014):

$$\text{Matrix bias (relative to SCO)} = 1000 \ln \left[\frac{1 + (\delta^{18}O^{*}(\text{reference}) / 1000)}{1 + (\delta^{18}O_{LF}(\text{reference}) / 1000)}\right] \quad (3)$$

Since San Carlos olivine is used to establish $\alpha^{18}O_{SIMS}$ (Eq. 1) it follows that (1) it has a matrix bias of 0‰ (Eq. 3), and (2) matrix bias values of all other olivine reference materials are calculated relative to that of San Carlos olivine (supplementary material, Table S1). Consequently, the matrix bias represents variations in the oxygen isotopic composition due to differences in the chemical composition of the olivine samples compared to San Carlos olivine. For most of the analysed olivine samples, the approximation equation 'Matrix bias $\approx \delta^{18}O^{*}$(reference) $- \delta^{18}O_{LF}$(reference) = $\Delta^{18}O_{SIMS\text{-}LF}$' (e.g., Hoefs, 2009) gave results that differed by ± 0.1‰ at the most compared to those calculated using Eq. (3). Nevertheless, matrix bias calculated in samples Fo_{99} and JUB (which have $\delta^{18}O$ values > 10‰; Table 2) using the α- and Δ-formats differed by ± 0.2‰ and ± 0.4‰, respectively. Consequently, the approximation equation was avoided in this study and all calculations were performed using Eq. (3). The final oxygen isotopic composition of each olivine unknown is calculated as follows (e.g., Martin et al., 2014):

$$\delta^{18}O_{V\text{-}SMOW} = \delta^{18}O^{*} \text{ (unknown)} - \text{Matrix bias} \quad (4)$$

The $\delta^{18}O_{V\text{-}SMOW}$ values of olivine unknowns rely on their Fo content, in order to determine the extent of the matrix bias (as detailed further in section 6.1).

4.2. Calculation of uncertainty on oxygen isotope measurements

The uncertainty of individual analyses (internal precision) is the weighted standard error (e), defined as:

$$e = \omega\sigma / \sqrt{N} \quad (5)$$

Where $\omega\sigma$ is the weighted standard deviation of the isotope ratios measured in each scan, and N is the number of scans (Ickert et al., 2008; Rubatto et al., 2014). The repeatability (i.e., spot-to-spot precision) of the analyses within a session is given by the standard deviation (SD) at 95% confidence level (c.l.) of the $\delta^{18}O$ values (Ickert et al., 2008). The external precision for each sample (σ) is given by:

$$\sigma = \sqrt{SE_U^2 + SE_S^2 + SE_R^2 + \sigma_{Fa}^2} \quad (6)$$

Where SE_U is the standard error of the sample analyses by SHRIMP, SE_S is the standard error of the reference material analyses by SHRIMP, SE_R is the uncertainty in the laser fluorination reference composition of the reference material and σ_{Fa} is the precision on the matrix bias correction. The latter is calculated as the residuals on the quadratic regression of $\delta^{18}O$ matrix bias on fayalite content (mole %) and is given by (e.g., Martin et al., 2014):

$$\sigma_{Fa} = \sqrt{\frac{\sum_{i=1}^{n} (bias - \widehat{bias})^2}{n-3}} \quad (7)$$

Where $bias$ is the measured matrix bias, $\widehat{bias}$ is the value of the matrix bias predicted by the quadratic regression, and n is the number of analyses used for the regression

(e.g., Martin et al., 2014, Rubatto et al., 2014). Consequently, σ_{Fa} indicates how far the measured bias is spread out from the regression curve, hence, how precise the matrix bias correction is. The quadratic sum of the residuals is divided by (n–3) because the matrix bias is described by a quadratic function, $ax^2 + bx + c$, where three unknown parameters (i.e., a, b, c) have to be estimated during the regression resulting in a loss of three degrees of freedom.

Unless otherwise specified, uncertainties on single analyses are 2e and uncertainties on average values σ are at 95% c.l. The 95% c.l. is calculated by multiplying SD and σ by Student's t factor, which is a function of the number of analyses.

5. RESULTS

Laser fluorination bulk analyses of synthetic forsterite Fo_{100} yielded $\delta^{18}O$ values of 5.49 ± 0.19‰ (1σ, n = 3). The analyses for the natural forsterite grains yielded $\delta^{18}O$ values of 23.20 ± 0.10‰ (1σ, n = 1) for Fo_{99} and 5.34 ± 0.09‰ (1σ, n = 2) for Fo_{93} (Table 2). Oxygen isotope reference values determined in the other olivine crystals by other studies are also shown in Table 2.

Ion microprobe oxygen isotope analyses of olivine were performed in four different sessions using both SHRIMP SI and SHRIMP II (supplementary material, Tables S1–S2). Between 27 and 236 analyses were performed in each of four analytical sessions and resulted in a repeatability (SD at 95% c.l.) ranging between ± 0.31‰ and ± 0.48‰ on San Carlos olivine (supplementary material, Table S2). Overall, the repeatability of the various olivine crystals was comparable to that of San Carlos olivine (Fig. 1; supplementary material, Tables S1–S2). A slight positive and a negative trend is observed in the matrix bias for < Fo_{90} and > Fo_{90}, respectively, even though for the

majority of the olivine reference materials (Fo_{74} to Fo_{93}) the extent of the matrix bias was within the analytical uncertainty of San Carlos olivine (Fig. 2; supplementary material, Tables S1–S2). The Mg-rich end-members (samples Fo_{99}, Fo_{100} and JUB) show matrix bias up to ~ –2‰ (Fig. 1, 2), which is well outside the precision of the oxygen analyses by ion microprobe. The trend in the matrix bias from Fo_{74} to Fo_{100} is reproducible at a level that is similar to the repeatability of measurements per sample, within a given session (~ ≤ 0.5‰, n = 2; Fig. 2). No obvious correlation was observed between IMF and $^{16}O^-$ secondary ion yields in San Carlos olivine (supplementary material, Fig. S1).

6. MATRIX BIAS

6.1. Correction scheme

The systematic matrix bias observed during the different analytical sessions along with the consistency of the results obtained using two different SHRIMP instruments suggest that variations in the Mg/Fe ratio are the major cause for the observed matrix bias in olivine. The variation of the matrix bias as a function of fayalite content (mole %) is best described by the following quadratic function (Fig. 2):

$$Bias_{Fa} = -0.0062\ Fa^2 + 0.233\ Fa - 1.60 \quad (8)$$

Where the fayalite content is expressed in mole %. The precision on the matrix bias correction, σ_{Fa}, is 0.22‰. The matrix bias correction is expressed in terms of fayalite content such that the intercept of the calibration curve coincides with the bias measured

in the forsterite end-members. For olivine with typical mantle compositions (Fo_{88}–Fo_{92}) the extent of matrix bias is negligible and thus no matrix bias correction should be applied when analysing these compositions against San Carlos olivine in order to avoid propagating a large uncertainty on the true oxygen isotope composition. Conversely, it is recommended to apply a matrix bias correction according to equation (8) for olivine characterised by forsterite contents in the range 74–88 mole % and > 92 mole % (Fig. 2).

6.2. Comparison with previous studies

Compositional matrix bias effects in olivine during oxygen isotope analyses by ion microprobe have previously been investigated using Cameca ion microprobes (e.g., Bindeman et al., 2008; Kita et al., 2010; Nakashima et al., 2013; Tenner et al., 2015; Isa et al., 2017). The most recent calibration by Isa et al. (2017) covered nearly the entire Mg–Fe olivine solid solution (from Fo_3 to Fo_{98}). The authors found a correlation between the magnitude of matrix bias and the sputtering rate that, in turn, depended on the Fe-content in olivine. In particular, under similar analytical conditions, they observed faster sputtering rates in Fe-rich compared to Mg-rich olivine resulting in larger magnitudes for the matrix bias (Fig. 3a). The calibration by Isa et al. (2017) confirmed lack of significant matrix bias effects in the compositional range Fo_{60} to Fo_{98} with the Cameca ion microprobes, in agreement with previous studies (Fig. 3; e.g., Bindeman et al., 2008; Kita et al., 2010; Nakashima et al., 2013; Tenner et al., 2015). Conversely, the calibration proposed in this study for the SHRIMP ion microprobes suggests a significant extent of matrix bias for olivine yielding forsterite contents larger than 92 mole % (Fig. 2,

3). Matrix bias effects for olivine appear more pronounced when approaching end-member compositions, and this characteristic of SHRIMP analysis occurs for other phases as well. In fact, Gauthiez-Putallaz et al. (2016) observed a matrix bias of ~ –1.4‰ when referencing analyses of pyrope PrpDM (pyrope: 99 mole %; grossular: 0 mole %; Vielzeuf et al., 2005) to UWG2 garnet (pyrope: 40 mole %; grossular: 14 mole %; Valley et al., 1995), after applying the correction for the grossular component proposed by Martin et al. (2014). The bias calculated by Gauthiez-Putallaz et al. (2016) agrees with the correlation between magnitude of matrix bias and molar volume of the other garnet end-members observed by Martin et al. (2014). These results suggest that different instrumental designs and/or analytical settings can significantly affect the magnitude of matrix bias (e.g., Tenner et al., 2013). Consequently, given this study did not investigate the potential influence of varying analytical settings on the magnitude of the matrix bias, it is recommended to keep monitoring matrix bias effects during every analytical session to corroborate the long-term reproducibility of the calibration equation (8). Additionally, more effort needs to be made in future to explore matrix bias effects in Fe-rich olivine samples to ascertain whether or not the magnitude of matrix bias would be larger compared to that observed for the forsterite end-member in the SHRIMP laboratories. It is, therefore, not recommended to extrapolate the calibration of the matrix bias provided in this study to olivine having forsterite contents lower than 74 mole %.

7. APPLICATION TO A SERPENTINISED DUNITE FROM THE NUASAHI MASSIF (EASTERN INDIA)

7.1. Geological background

The Nuasahi ultramafic massif (outcrop area ~ 10 km^2) is located in eastern India and it forms a sill-like layered intrusive complex within the Iron Ore Group supracrustal sequence of an Archean greenstone belt (Mondal et al., 2001; 2006; Majumdar et al., 2016). It consists of three main magmatic suites distinguished on the basis of their intrusion age (Mondal et al., 2001): (1) suite 1 is made of layered ultramafic rocks consisting of dunites, orthopyroxenites, harzburgites and chromitites, (2) suite 2 is a gabbro-anorthosite intrusive within suite 1, (3) suite 3 is the youngest magmatic suite made of dolerites, clinopyroxenites, gabbros and quartz-diorites intruding the older magmatic suites. In particular, the Bangur gabbro represents the youngest magmatic episode (3121 ± 3 Ma) recorded in the area (Augé and Lerouge, 2004 and references therein). According to Mondal et al. (2006), the chromitites together with their host ultramafic rocks of suite 1 crystallised from a mantle-derived boninitic or siliceous high-Mg basaltic magma that intruded the volcano-sedimentary greenstone-belt. The investigated dunite belongs to suite 1, has an approximate lateral thickness of ~ 130–150 metres and hosts three major stratiform chromitite layers. It is in sharp, but non-intrusive contact on both sides with orthopyroxenite layers having a thickness of ~ 20–140 metres. The ultramafic unit is, in turn, flanked on both sides by the gabbro-anorthosite constituting suite 2 (Majumdar et al., 2016). For more details on the field

445 relationships see Mondal et al. (2001; 2006), Augé and Lerouge (2004), Majumdar et
446 al. (2016).
447
448 7.2. Sample description
449
450 The serpentinised dunite investigated in this study was provided by Prof. Sisir K.
451 Mondal (Jadavpur University, India). The sample has previously been
452 characterised for its microtextural-chemical evolution by Majumdar et al. (2016).
453 The dunite mainly consists of olivine, lizardite, brucite, magnetite, chromite and
454 magnesite. Lizardite was characterised by Raman spectroscopy and has a homogenous
455 major element composition with an Mg# of 0.95 (Table 3). Olivine crystals are zoned
456 (Fig. 4) and are characterised by a core with typical mantle chemical compositions
457 (Fo_{92}) and a rim enriched in the forsterite component (Fo_{98}) (Table 3).
458 According to Majumdar et al. (2016), primary olivine crystals were replaced by a
459 $lizardite_1$ + brucite + magnetite assemblage during a first stage of serpentinisation at T
460 ≤ 300°C, which resulted in the development of a pseudomorphic mesh texture (Fig. 4a–
461 b). This first stage of serpentinisation was followed by the precipitation of a brucite-
462 free $lizardite_2$ layer at the interface with the olivine crystals, which could have resulted
463 either from an increase in silica activity in the reacting solution (due to the activation
464 of a volume-conservative serpentinisation reaction that releases SiO_2) or from a
465 decrease in temperature in the system (Fig. 4). Finally, the development of Mg-rich
466 pseudomorphic olivine rims replacing primary olivine cores at the inner interface of the
467 brucite-free lizardite layers is attributed to a decrease in the silica and/or water activity
468 plus an increase in Mg^{2+}/Fe^{2+} proportion in the reacting solution.

The high B content measured in lizardite (~ 20–32 ppm) and Mg-rich olivine rims (6.9–10 ppm) compared to olivine cores (0.84–2.5 ppm) as well as the decoupled behaviour of B and Li variations between the two olivine generations and serpentine have been interpreted as the result of seafloor alteration of the Nuasahi dunites (Majumdar et al., 2016). Based on petrographic observations as well as chemical and bulk stable isotope (O, H, S) geochemistry, Augé and Lerouge (2004) also attributed the late stage of alteration observed in the apophysis of the Bangur gabbro intrusion to interaction with externally derived surface fluids. This is distinct from high-temperature magmatic fluids released during crystallisation of the gabbro that were, instead, responsible for three earlier stages of alteration (Augé and Lerouge, 2004).

Given the complexity of the compositional zoning observed in olivine, the nature and source(s) of the fluid(s) responsible for serpentinisation in the dunite from the Nuasahi massif are best investigated by *in situ* analysis of oxygen isotopes in both olivine cores and rims. Additionally, based on the new analytical development discussed in Scicchitano et al. (2018), further constraints on this process can be obtained by the simultaneous analysis of oxygen isotopes at the microscale in the lizardite surrounding the olivine crystals.

7.3. Oxygen isotope compositions of olivine and lizardite

Olivine and brucite-free lizardite domains in the partly serpentinised dunite from the Nuasahi massif were analysed for oxygen isotopes at the microscale by SHRIMP SI (supplementary material, Tables S3–S4). Analyses of olivine cores and rims were referenced to San Carlos olivine (Fo_{91}; $\delta^{18}O = 5.27 \pm 0.10‰$; Eiler et al., 1995; 2000; Bindeman et al., 2008; Ahn et al., 2012; Isa et al., 2017) and analyses of lizardite were

494 referenced to the antigorite reference material Al06-44A (Mg# 0.95, $\delta^{18}O$ = 8.30 ±
495 0.12‰; Scicchitano et al., 2018) because no other serpentine reference materials were
496 available at the time. Scicchitano et al. (2018) observed a systematic matrix bias of ~ –
497 0.8‰ between antigorite Al06-44A and the lizardite reference material L3431 (Mg#
498 0.98) and negligible matrix bias effects between antigorite Al06-44A and the chrysotile
499 reference material C22908 (Mg# 0.98; supplementary material, Fig. S2). Because the
500 bias between antigorite and lizardite cannot be unequivocally attributed to the different
501 Mg/Fe ratio in the two phases (but could also result from their different crystal
502 structure), analyses on the Nuasahi lizardite (Mg# 0.95; Table 3) were corrected for the
503 bias measured between antigorite Al06-44A and lizardite L3431 (i.e., –0.8‰) despite
504 the latter having a higher Mg/Fe ratio. The uncertainty on the matrix bias correction of
505 the Nuasahi lizardite due to its lower Mg/Fe ratio compared to the reference material
506 L3431 was taken into account for the calculation of its oxygen isotope composition as
507 well as for estimating the equilibrium temperature and the $\delta^{18}O$ composition of the fluid
508 (as detailed further below and in section 7.4.). Analyses of olivine rims, which are
509 significantly richer in Mg than San Carlos olivine, were corrected for the matrix bias
510 according to equation (8), whereas the matrix bias correction was not applied to analysis
511 on olivine cores that have typical mantle chemical compositions and are close in
512 composition to San Carlos olivine (see discussion above).
513 The repeatability (SD at 95% c.l.) on San Carlos olivine and antigorite Al06-44A was
514 ± 0.35‰ (n = 22) and ± 0.43‰ (n = 11), respectively (Fig. 5a; supplementary material,
515 Table S4). Olivine cores and rims have oxygen isotopic compositions of 5.16 ± 0.30‰
516 (σ at 95% c.l.) and 1.92 ± 0.60‰ (σ at 95% c.l.), respectively (Fig. 5b). Brucite-free
517 lizardite$_2$ domains have an oxygen isotopic composition of 4.87 ± 0.53‰ (σ at 95% c.l.;
518 Fig. 5b), if matrix bias correction is applied. Nevertheless, given the brucite-free

519 lizardite has a lower Mg# than the lizardite reference material L3431, its oxygen
520 isotopic composition could be slightly lower than that measured if the matrix bias effect
521 related to Mg/Fe variation in serpentine is comparable to that observed in olivine. In
522 the extreme case scenario that no matrix bias effects existed between the Nuasahi
523 lizardite and the antigorite reference material Al06-44A, because of their similar Mg/Fe
524 ratios, the brucite-free lizardite$_2$ would have a $\delta^{18}O$ composition of 4.07 ± 0.53‰ (σ at
525 95% c.l.; supplementary material, Table S3). The contrasting composition of olivine
526 core and rim and of lizardite can be measured in grains that are texturally adjacent to
527 each other (Fig. 4c).
528
529 7.4. Temperature of serpentinisation and source of fluids in the Nuasahi dunite
530
531 The olivine cores have oxygen isotopic compositions (5.16 ± 0.30‰) comparable to
532 those of olivine crystals typically encountered in mantle peridotites (5.18 ± 0.28‰,
533 2SD; Mattey et al., 1994). We thus interpret the olivine core as relicts of the magmatic
534 stage, in agreement with their chemical composition (Majumdar et al., 2016).
535 The oxygen isotopic composition of the brucite-free lizardite domains (4.07–4.87 ±
536 0.53‰) falls within the range typically observed in serpentinites and serpentine
537 minerals currently forming in mid-ocean ridge environments, which peak at 2 to 5‰
538 (e.g., Mével, 2003). The oxygen isotopic fractionation of ~ 3‰ measured between
539 lizardite (4.87 ± 0.53‰) and olivine rims (1.92 ± 0.60‰) suggests that the two minerals
540 are locally in equilibrium at ~ 405–430°C (Fig. 6a), considering the uncertainty on the
541 $\delta^{18}O$ values of both lizardite and olivine rim. For this calculation we used the mineral–
542 fluid fractionation factors by Zheng (1993a; 1993b) for internal consistency; in these *T*
543 ranges the factors of Zheng (1993a) are similar to what proposed by Richter and

Hoernes (1988) for forsterite–water. The calculated values would represent a minimum equilibrium temperature if a matrix bias effect related to Mg/Fe variation in serpentine was to be confirmed. Conversely, if no matrix bias effects are assumed between the Nuasahi lizardite and the antigorite reference material Al06-44A, the oxygen isotope fractionation of ~ 2‰ between lizardite$_2$ (4.07 ± 0.53‰) and olivine rims (1.92 ± 0.60‰) would result in an equilibrium temperature of ~ 570–610°C (Fig. 6a), taking into account the uncertainties on the $\delta^{18}O$ values of both minerals (calculated from mineral–fluid fractionation factors by Zheng, 1993a; 1993b). Although lizardite is usually stable at $T \leq 300$°C in the MSH system (Evans, 2004), this serpentine polymorph has been observed in natural samples up to ~ 390°C (e.g., Schwartz et al., 2013). Additionally, experimental studies (e.g., Chernosky, 1973; Caruso and Chernosky, 1979) have shown that the thermal stability of lizardite increases up to ~ 600°C with increasing alumina content (Al_2O_3 up to ~ 9.2 wt.%; Andreani et al., 2007). The lizardite in the serpentinised dunite from the Nuasahi massif is poor in alumina (i.e., Al_2O_3 = 0.23 wt.%; Majumdar et al., 2016) and thus it is unlikely that this led to an increased thermal stability. However it is possible that other trivalent cations commonly encountered in serpentine minerals (e.g., Fe^{3+}; e.g., Mellini, 1982; Evans, 2008; Debret et al., 2015) might have a similar effect in stabilising lizardite to higher temperatures. Nevertheless, it is important to point out that the highest metamorphic grade recorded in the area corresponds to greenschist facies conditions and no amphibolite overprints are observed (Majumdar et al., 2016). Consequently, the oxygen isotope data suggest local oxygen isotopic equilibration between brucite-free lizardite and olivine rims at temperatures of ~ 405–430°C, which is also consistent with lack of antigorite in the sample. Olivine rims have a Mg# higher than brucite-free lizardite, conversely to what is observed in high-pressure serpentinites (e.g., Trommsdorff and

569 Evans, 1972). This indicates that olivine rims were not the result of a de-
570 serpentinisation process but are likely the result of more complex fluid-rock
571 interactions, as also suggested by the textural relations between the phases. Our oxygen
572 isotopic data constrain only the second serpentinisation stage described by Majumdar
573 et al. (2016), responsible for the formation of brucite-free lizardite and olivine rims.
574 The oxygen isotope composition of the first serpentinisation stage is more difficult to
575 obtain due to the fine-grained intergrowth of lizardite and brucite and to potential
576 crystal orientation effects during *in situ* analysis of oxygen isotopes in magnetite (e.g.,
577 Huberty et al., 2010).
578 A fluid with $\delta^{18}O$ composition between 5.3‰ and 6.9‰ (fractionation factors after
579 Zheng, 1993b and Früh-Green et al., 1996; Fig. 6b) would be in equilibrium with this
580 lizardite at 405–430°C (considering the uncertainty on the $\delta^{18}O$ value). A comparable
581 oxygen isotopic composition of ~ 5.3–6.5‰ is calculated for the fluid in equilibrium
582 with the olivine rims in the same temperature range (Fig. 6b; fractionation factors after
583 Zheng, 1993a). A similar $\delta^{18}O$ fluid of ~ 5.1–6.4‰ is calculated if an equilibrium
584 temperature of ~ 570-610°C is assumed between lizardite$_2$ and olivine rim (no matrix
585 bias correction in lizardite; Fig. 6b; fractionation factors after Zheng, 1993a; 1993b).
586 Consequently, only seawater heavily enriched in ^{18}O by isotopic exchange during
587 infiltration (e.g., Putlitz et al., 2001) could have been responsible for the second
588 serpentinisation stage observed in the Nuasahi dunite as suggested by Majumdar et al.
589 (2016) on the basis of trace element compositions.
590
591 8. CONCLUSIONS
592

593 This study reports the first investigation of matrix bias effects related to variations of
594 Mg/Fe in olivine during *in situ* analysis of oxygen isotopes by SHRIMP ion
595 microprobes, and the application of the correction scheme to a partly serpentinised
596 dunite to unravel the nature and source of the serpentinising fluids as well as the
597 temperature of serpentinisation.

598 • Matrix bias effects from +0.7‰ to –2‰ were observed in olivine samples having
599 forsterite contents ranging from 74 to 100 mole %.

600 • The variation of the matrix bias as a function of fayalite content (mole %) is best
601 described by the quadratic function: $Bias_{Fa} = -0.0062\ Fa^2 + 0.233\ Fa - 1.60$.

602 • *In situ* oxygen isotope analysis of zoned olivine crystals (Fo_{92} cores and Fo_{98}
603 rims) and surrounding brucite-free lizardite domains in a partly serpentinised
604 dunite from the Archean Nuasahi massif suggests that (i) olivine cores are relicts
605 of the magmatic stage, (ii) olivine rims and brucite-free lizardite formed during
606 serpentinisation at ~ 405–430°C as a result of interaction with seawater enriched
607 in ^{18}O by isotopic exchange during infiltration.

608

ACKNOWLEDGEMENTS

The authors are grateful to all the colleagues who made this research possible by kindly sharing their samples: Christoph Beier (Universität Erlangen-Nürnberg) and Felix Genske (Universität Münster) provided samples S3, SJ6 and P29; Peter Tollan (University of Bern) provided samples VS2A, VS18 and 6702-B1; Lukas Baumgartner and Benita Putlitz (University of Lausanne) provided sample JUB; Hugh O'Neill (Australian National University) provided sample Fo_{100}; Michael Jollands (University of Lausanne) provided samples Fo_{93} and Fo_{99}; Sisir K. Mondal (Jadavpur University, India) provided the partly serpentinised dunite sample. The Centre of Advanced Microscopy (ANU) is acknowledged for access to the SEM facilities. We would like to thank Pierre Lanari (University of Bern) for assistance during EMPA analyses; Peter Holden and Janaina Avila (RSES, ANU) for help during SHRIMP analyses; Peter Tollan, Lukas Baumgartner, Benita Putlitz and Yong-Fei Zheng (University of Science and Technology of China in Hefei) for providing laser fluorination analyses. Ian Williams and an anonymous reviewer of the PhD thesis of M.R.S. helped improve an early version of this work. We also acknowledge three anonymous reviewers for their thorough and constructive comments on the manuscript, and Catherine Chauvel for editorial handling. DR acknowledges the financial support of the Australian Research Council (DP110101599) and the Swiss National Science Foundation (SNSF 200021_166280).

629 REFERENCES

630 Ahn, I., Lee, J.I., Kusakabe, M., Choi, B.-G., 2012. Oxygen isotope measurements of terrestrial silicates
631 using a CO_2-laser BrF_5 fluorination technique and the slop of terrestrial fractionation line.
632 Geosciences Journal 16(1), 7-16.

633 Andreani M., Mével, C., Boullier, A.-M., Escartín, J., 2007. Dynamic control on serpentine
634 crystallization in veins: Constraints on hydration processes in oceanic peridotites. Geochemistry,
635 Geophysics, Geosystems 8(2), 1-24.

636 Augé T., Lerouge, C., 2004. Mineral-chemistry and stable-isotope constraints on the magmatism,
637 hydrothermal alteration, and related PGE-(base-metal sulphide) mineralisation of the Mesoarchaean
638 Baula-Nuasahi Complex, India. Mineralium Deposita 39, 583-607.

639 Baertschi, P., 1976. Absolute ^{18}O content of standard mean ocean water. Earth and Planetary Science
640 Letters 31, 341-344.

641 Bindeman, I., Gurenko, A., Sigmarsson, O., Chaussidon, M., 2008. Oxygen isotope heterogeneity
642 and disequilibria of olivine crystals in large volume Holocene basalts from Iceland: Evidence
643 for magmatic digestion and erosion of Pleistocene hyaloclastites. Geochimica et Cosmochimica
644 Acta 72, 4397-4420.

645 Bindeman, I., Sigmarsson, O., Eiler, J., 2006. Time constraints on the origin of large volume
646 basalts derived from O-isotopes and trace element mineral zoning and U-series disequilibria in
647 the Laki and Grímsvötn volcani system. Earth and Planetary Science Letters 245, 245-259.

648 Byerly, B.L., Kareem, K., Bao, H., Byerly, G.R., 2017. Early Earth mantle heterogeneity revealed
649 by light oxygen isotopes of Archaean komatiites. Nature Geoscience 10, 871-876.

650 Caruso, L.J., Chernosky, J.V., 1979. The stability of lizardite. Canadian Mineralogist 17, 757-769.

651 Chaussidon, M., Libourel, G., Krot, A.N., 2008. Oxygen isotopic constraints on the origin of
652 magnesian chondrules and on the gaseous reservoirs in the early Solar System. Geochimica et
653 Cosmochimica Acta 72, 1924-1938.

654 Chazot, G., Lowry, D., Menzies, M., Mattey, D., 1997. Oxygen isotopic composition of hydrous
655 and anhydrous mantle peridotites. Geochimica et Cosmochimica Acta 61(1), 161-169.

656 Chernosky, J.V., 1973. An experimental investigation of the serpentine and chlorite group minerals in
657 the system MgO-Al_2O_3-SiO_2-H_2O. Ph.D. thesis, Mass. Inst. Tech., Cambridge.

Coplen, T.B., Kendall, C., Hopple, J., 1983. Comparison of stable isotope reference samples. Nature 302, 236-238.

Debret, B., Bolfan-Casanova, N., Padrón-Navarta, J.A., Martin-Hernandez, F., Andreani, M., Garrido, C.J., Sánchez-Vizcaíno, V.L., Gómez-Pugnaire, M.T., Muñoz, M., Trcera, N., 2015. Redox state of iron during high-pressure serpentinite dehydration. Contribution to Mineralogy and Petrology 169, 36 DOI 10.1007/s00410-015-1130-y.

Deines, P., Haggerty, S.E., 2000. Small-scale oxygen isotope variations and petrochemistry of ultradeep (> 300 km) and transition zone xenoliths. Geochimica et Cosmochimica Acta 64(1), 117-131.

Deloule, E., France-Lanord, C., Albarède, F., 1991. D/H analysis of minerals by ion probe. In *Stable Isotope Geochemistry: A tribute to Samuel Epstein* (eds. H.P. Taylor Jr., J.R. O'Neil and I.R. Kaplan), pp. 53-62. The Geochemical Society, Special Publication No. 3. San Antonio.

Eiler, J.M., 2001. Oxygen isotope variations of basaltic lavas and upper mantle rocks. Review in Mineralogy and Geochemistry 43, 319-364.

Eiler, J.M., Farley, K.A., Valley, J.W., Stolper, E.M., Hauri, E.H., Craig, H., 1995. Oxygen isotope evidence against bulk recycled sediment in the mantle sources of Pitcairn Island lavas. Nature 377, 138-141.

Eiler, J.M., Graham, C., Valley, J.W., 1997. SIMS analysis of oxygen isotopes: matrix effects in complex minerals and glasses. Chemical Geology 138, 221-244.

Eiler, J.M., Grönvold, K., Kitchen, N., 2000. Oxygen isotope evidence for the origin of chemical variations in lavas from Theistareykir volcano in Iceland's northern volcanic zone. Earth and Planetary Science Letters 184, 269-286.

Evans, B.W., 2004. The Serpentinite Multisystem Revisited: Chrysotile Is Metastable. International Geology Review 46, 479-506.

Evans, B.W., 2008. Control of the product of serpentinization by the $Fe^{2+}Mg_{-1}$ exchange potential of olivine and orthopyroxene. Journal of Petrology 49(10), 1873-1887.

Früh-Green, G.L., Plas, A., Lécuyer, C., 1996. Petrologic and stable isotope constraints on hydrothermal alteration and serpentinization of the EPR shallow mantle at Hess Deep (site 895). Proceedings of the Ocean Drilling Program, Scientific Results 147, 255-291.

687 Gauthiez-Putallaz, L., Rubatto, D., Hermann, J., 2016. Dating prograde fluid pulses during
688 subduction by in situ U-Pb and oxygen isotope analysis. Contribution to Mineralogy and
689 Petrology 171, 15 DOI 10.1007/s00410-015-1226-4
690 Genske, F.S., Beier, C., Haase, K.M., Turner, S.P., Krumm, S., Brandl, P.A., 2013. Oxygen isotopes in
691 the Azores islands: crustal assimilation recorded in olivine. Geology DOI: 10.1130/G33911.1
692 Gong, B., Zheng, Y.-F., Chen, R.-X., 2007. TC/EA-MS online determination of hydrogen isotope
693 composition and water concentration in eclogitic garnet. Physics and Chemistry of Minerals 34(10),
694 687-698.
695 Gurenko, A.A., Chaussidon, M., 2002. Oxygen isotope variations in primitive tholeiites of Iceland:
696 evidence from a SIMS study of glass inclusions, olivine phenocrysts and pillow rim glasses.
697 Earth and Planetary Science Letters 205, 63-79.
698 Hoefs, J., 2009. Stable isotope geochemistry. Springer (Berlin), 293pp.
699 Huberty, J.M., Kita, N.T., Kozdon, R., Heck, P.R., Fournelle, J.H., Spicuzza, M.J., Xu, H., Valley, J.W.,
700 2010. Crystal orientation effects in $\delta^{18}O$ for magnetite and hematite by SIMS. Chemical Geology
701 276, 269-283.
702 Ickert, R.B., Hiess, J., Williams, I.S., Holden, P., Ireland, T.R., Lanc, P., Schram, N., Foster, J.J.,
703 Clement, S.W., 2008. Determining high precision, in situ, oxygen isotope ratios with a *SHRIMP II*:
704 Analyses of MPI-DING silicate-glass reference materials and zircon from contrasting granites.
705 Chemical Geology 257(1-2), 114-128.
706 Ireland, T.R, Clement, S., Compston, W., Foster, J.J., Holden, P., Jenkins, B., Lanc, P., Schram, N.,
707 Williams, I.S., 2008. Development of SHRIMP. Australian Journal of Earth Sciences 55, 937-954.
708 Isa, J., Kohl, I.E., Liu, M.-C., Wasson, J.T., Young, E.D., McKeegan, K.D., 2017. Quantification
709 of oxygen isotope SIMS matrix effects in olivine samples: Correlation with sputter rate.
710 Chemical Geology 458, 14-21.
711 Kita, N.T., Ushikubo, T., Fu, B., Valley, J.W., 2009. High precision SIMS oxygen isotope analysis and
712 the effect of sample topography. Chemical Geology 264, 43-57.
713 Kita, N.T., Nagahara, H., Tachibana, S., Tomomura, S., Spicuzza, M.J., Fournelle, J.H., Valley,
714 J.W., 2010. High precision SIMS oxygen three isotope study of chondrules in LL3 chondrites:
715 Role of ambient gas during chondrule formation. Geochimica et Cosmochimica Acta 74, 6610-
716 6635.

717 Lacroix, B., Vennemann, T., 2015. Empirical calibration of the oxygen isotope fractionation
718 between quartz and Fe-Mg chlorite. Geochimica et Cosmochimica Acta 149, 21-31.
719 Majumdar, A.S., Hövelmann, J., Vollmer, C., Berndt, J., Mondal, S.K., Putnis, A., 2016. Formation of
720 Mg-rich olivine pseudomorphs in serpentinized dunite from the Mesoarchaean Nuasahi Massif,
721 Eastern India: insights into the evolution of fluid composition at the mineral-fluid interface. Journal
722 of Petrology 57(1), 3-26.
723 Martin, L.A.J., Rubatto, D., Crépisson, C., Hermann, J., Putlitz, B., Vitale-Brovarone, A., 2014. Garnet
724 oxygen analysis by SHRIMP-SI: Matrix correction and application to high-pressure metasomatic
725 rocks from Alpine Corsica. Chemical Geology 374-375, 25-36.
726 Mattey, D., Lowry, D., Macpherson, C., 1994. Oxygen isotope composition of mantle peridotite.
727 Earth and Planetary Science Letters 128, 231-241.
728 Mellini, M., 1982. The crystal structure of lizardite-1T: Hydrogen bonds and polytypism. American
729 Mineralogist 67, 587-598.
730 Mével, C., 2003. Serpentinization of abyssal peridotites at mid-ocean ridges. C.R. Geoscience 335, 825-
731 852.
732 Mondal, S.K., Baidya, T.K., Gururaja Rao, K.N., Glascock, M.D., 2001. PGE and Ag mineralization in
733 a breccia zone of the Precambrian Nuasahi ultramafic-mafic complex, Orissa, India. Canadian
734 Mineralogist 39, 979-996.
735 Mondal, S.K., Ripley, E.M., Li, C., Frei, R., 2006. The genesis of Archaean chromitites from the Nuasahi
736 and Sukinda massifs in the Singhbhum Craton, India. Precambrian Research 148, 45-66.
737 Nakashima, D., Kita, N.T., Ushikubo, T., Noguchi, T., Nakamura, T., Valley, J.W., 2013. Oxygen
738 three-isotope ratios of silicate particles returned from asteroid Itokawa by the Hayabusa
739 spacecraft: A strong link with equilibrated LL chondrites. Earth and Planetary Science Letters
740 379, 127-136.
741 Page, F.Z., Kita, N.T., Valley, J.W., 2010. Ion microprobe analysis of oxygen isotopes in garnets of
742 complex chemistry. Chemical Geology 270, 9-19.
743 Putlitz, B., Katzir, Y., Matthews, A., Valley, J.W., 2001. Oceanic and orogenic fluid-rock interaction in
744 $^{18}O/^{16}O$-enriched metagabbros of an ophiolite (Tinos, Cyclades). Earth and Planetary Science Letters
745 193, 99-113.

746 Richter, R., Hoernes, S., 1988. The application of the increment method in comparison with
747 experimentally derived and calculated O-isotope fractionations. Chemie der Erde 48, 1-18.
748 Rollion-Bard, C., Marin-Carbonne, J., 2011. Determination of SIMS matrix effects on oxygen isotopic
749 compositions in carbonates. Journal of Analytical Atomic Spectrometry 26, 1285-1289.
750 Roselle, G.T., Baumgartner, L.P., Valley, J.W., 1999. Stable isotope evidence of heterogenous fluid
751 infiltration at the Ubehebe peak contact aureole, Death Valley National Park, California. American
752 Journal of Science 299, 93-138.
753 Rubatto, D., Putlitz, B., Gauthiez-Putallaz, L., Crépisson, C., Buick, I.S., Zheng, Y.-F., 2014.
754 Measurment of in-situ oxygen isotope ratios in monazite by SHRIMP ion microprobe: Standards,
755 protocols and implications. Chemical Geology 380, 84-96.
756 Schwartz, S., Guillot, S., Reynard, B., Lafay, R., Debret, B., Nicollet, C., Lanari, P., Auzende, A.L.,
757 2013. Pressure-temperature estimates of the lizardite/antigorite transition in high pressure
758 serpentinites. Lithos 178, 197-210.
759 Shimizu, N., Hart, S.R., 1982. Isotope fractionation in secondary ion mass spectrometry. Journal of
760 Applied Physics 53, 1303-1311.
761 Scicchitano, M.R., Rubatto, D., Hermann, J., Shen, T., Padrón-Navarta, J.A., Williams, I.S., Zheng, Y.-
762 F., 2018. *In situ* oxygen isotope determination in serpentine minerals by ion microprobe: reference
763 materials and applications to ultrahigh-pressure serpentinites. Geostandards and Geoanalytical
764 Research DOI: 10.1111/ggr.12232
765 Śliwiński, M.G., Kitajima, K., Kozdon, R., Spicuzza, M.J., Fournelle, J.H., Denny, A., Valley, J.W.,
766 2016. Secondary Ion Mass Spectrometry Bias on Isotope Ratios in Dolomite-Ankerite, Part I: $\delta^{18}O$
767 Matrix Effects. Geostandards and Geoanalytical Research 40(2), 157-172.
768 Tenner, T.J., Nakashima, D., Ushikubo, T., Kita, N.T., Weisberg, M.K., 2015. Oxygen isotope
769 ratios of FeO-poor chondrules in CR3 chondrites: Influence of dust enrichment and H_2O during
770 chondrule formation. Geochimica et Cosmochimica Acta 148, 228-250.
771 Tenner, T.J., Ushikubo, T., Kurahashi, E., Kita, N.T., Nagahara, H., 2013. Oxygen isotope
772 systematics of chondrule phenocrysts from the CO3.0 chondrite Yamato 81020: Evidence fro
773 two distinct oxygen isotope reservoirs. Geochimica et Cosmochimica Acta 102, 226-245.
774 Tollan, P.M.E., 2014. A tale of two arcs: Petrogenesis of ultramafic xenoliths sampling the upper mantle
775 wedge beneath the west Bismarck island arc. Ph.D. thesis, Durham University.

776 Tollan, P.M.E., Bindeman, I., Blundy, J.D., 2012. Cumulate xenoliths from St. Vincent, Lesser Antilles
777 Island Arc: a window into upper crustal differentiation of mantle-derived basalts. Contribution to
778 Mineralogy and Petrology 163(2), 189-208.
779 Tollan, P.M.E., Dale, C.W., Hermann, J., Davidson, J.P. Arculus, R.J., 2017. Generation and
780 modification of the mantle wedge and lithosphere beneath the west Bismarck island arc: melting,
781 metasomatism and thermal history of peridotite xenoliths from Ritter Island. Journal of Petrology
782 58(8), 1475-1510.
783 Trommsdorff, V., Evans, B.W, 1972. Progressive metamorphism of antigorite schist in the Bergell
784 tonalite aureole (Italy). American Journal of Science 272, 423-437.
785 Ushikubo, T., Kimura, M., Kita, N.T., Valley, J.W., 2012. Primordial oxygen isotope reservoirs
786 on the solar nebula recorded in chondrules in Acfer 094 carbonaceous chondrite. Geochimica
787 et Cosmochimica Acta 90, 242-264.
788 Valley, J.W., Kita, N.T., 2009. *In situ* oxygen isotope geochemistry by ion microprobe. In: Fayek, M.
789 (Ed.), GAC/MAC Short Course: Secondary Ion Mass Spectrometry in the Earth and Planetary
790 Sciences 41, 19–63.
791 Valley, J.W., Kitchen, N., Kohn, M.J., Niendorf, C.R., Spicuzza, M.J., 1995. UWG-2, a garnet standard
792 for oxygen isotope ratios: strategies for high precision and accuracy with laser heating. Geochimica
793 et Cosmochimica Acta 59(24), 5223-5231.
794 Vielzeuf, D., Champenois, M., Valley, J.W., Brunet, F., Devidal, J.L., 2005. SIMS analyses of oxygen
795 isotopes: Matrix effects in Fe-Mg-Ca garnets. Chemical Geology 223, 208-226.
796 Zha, X.-P., Zhao, Y.-Y., Zheng, Y.-F., 2010. An online method combining a Gasbench II with continuous
797 flow isotope ratio mass spectrometry to determine the content and isotopic compositions of minor
798 amounts of carbonate in silicate rocks. Rapid Communications in Mass Spectrometry 24, 2217-2226.
799 Zhang, H.-F, Mattey, D.P., Grassineau, N., Lowry, D., Brownless, M., Gurney, J.J., Menzies, M.A.,
800 2000. Recent fluid processes in the Kaapvaal Craton, South Africa: coupled oxygen isotopes
801 and trace element disequilibrium in polymict peridotites. Earth and Planetary Science Letters
802 176, 57-72.
803 Zheng, Y.-F, 1993a. Calculation of oxygen isotope fractionation in anhydrous silicate minerals.
804 Geochimica et Cosmochimica Acta 57, 1079-1091.

805 Zheng, Y.-F., 1993b. Calculation of oxygen isotope fractionation in hydroxyl-bearing silicates. Earth
806 and Planetary Science Letters 120, 247-263.
807

FIGURE AND TABLE CAPTIONS

Fig. 1. SHRIMP oxygen isotope measurements of olivine reference materials of different Fe-Mg composition referenced to San Carlos olivine (Fo_{91}). Note that isotope ratios are only corrected for IMF ($\delta^{18}O^*$) to show the extent of matrix bias. The red lines represent laser fluorination reference values for the olivine reference materials. A systematic matrix bias that shifted by ~ ± 0.56‰ at the most over the various analytical sessions was observed in all samples. Grey bands are SD at 95% c.l of the SHRIMP values. Error bars on individual analyses are 2*e*.

Fig. 2. Relationship between forsterite content in olivine and the extent of matrix bias during oxygen isotope analyses with the SHRIMP ion microprobes. The matrix bias is negligible in the compositional range Fo_{88}-Fo_{92} and becomes significant in Mg-rich end-members (> Fo_{92}) as well as in the compositional range Fo_{74}–Fo_{88}. Error bars are SE at 95% c.l. and dashed red lines indicate the 95% confidence interval for the calibration curve. SCO = San Carlos olivine.

Fig. 3. (a) Comparison of matrix bias as a function of forsterite content during oxygen isotope analysis in olivine between different studies. (b) Significant matrix bias is observed in this study using a SHRIMP instrument for Fo > 92 mole %. Error bars are SE at 95% c.l. The data published in Kita et al. (2010), Nakashima et al. (2013), Tenner et al. (2015) and Isa et al. (2017) were used to calculate the SE at 95% c.l. for their average values to allow a consistent comparison with the data shown in this study.

Fig. 4. BSE images of the serpentinised dunite from the Nuasahi massif showing zoned olivine crystals surrounded by $lizardite_1$+brucite±magnetite (a, b) as well as brucite-free $lizardite_2$ domains (a–c). Olivine cores have typical mantle compositions (Fo_{92}), whereas the rims are enriched in the forsterite end-member (Fo_{98}; Table3). (c) Example of SHRIMP pits on adjacent olivine core, olivine rim and $lizardite_2$ along with the measured oxygen isotopic compositions ($\delta^{18}O_{V\text{-}SMOW}$ ‰). (d) Example of SHRIMP pit on a $lizardite_2$ domain with the corresponding $\delta^{18}O_{V\text{-}SMOW}$ value (‰). Ol_C = olivine core, Ol_R = olivine rim, Lz = lizardite, Mag = magnetite, Brc = brucite.

Fig. 5. SHRIMP oxygen isotope measurements of (a) San Carlos olivine (SCO) and antigorite reference material Al06-44A, (b) olivine cores (Ol_C), olivine rims (Ol_R) and lizardite (Lz) in the Nuasahi dunite. Grey bands are (a) SD at 95% c.l. for the reference materials and (b) σ at 95% c.l of the samples measurements.

Fig. 6. (a) Oxygen isotopic fractionation between serpentine and forsterite as a function of temperature calculated using the mineral-fluid fractionation factors by Zheng (1993a, 1993b). The oxygen isotopic signatures measured in lizardite and olivine rims in the Nuasahi dunite are consistent with equilibrium isotopic fractionation in the temperature range of ~ 405–430°C, if matrix bias correction on lizardite is applied. An equilibrium temperature of ~ 570–610°C is calculated if oxygen isotopic ratios in lizardite are not corrected for the matrix bias effects relative to antigorite Al06-44A (see text for details). (b) Oxygen isotopic compositions of a fluid in equilibrium with $lizardite_2$ (both corrected and uncorrected for matrix bias effects relative to antigorite Al06-44A) and olivine rims in the Nuasahi dunite calculated over the temperature range 100–610°C using the mineral-fluid fractionation factors by Zheng (1993a, 1993b). A fluid having an oxygen isotopic composition of ~ 5.3–6.9‰ and ~ 5.1–6.4‰ would be in equilibrium with both $lizardite_2$ and olivine rims at ~ 405–430°C and ~ 570–610°C, respectively (see text for details).

Table 1. Representative major element chemical compositions (wt.%) of the olivine reference materials. Cations are based on four oxygens.

Table 2. Mole% of forsterite end-member and reference bulk oxygen isotope compositions by laser fluorination for the olivine reference materials investigated for matrix bias in this study.

Table 3. Representative major element chemical compositions (wt.%) of olivine core, olivine rim and $lizardite_2$ from the Nuasahi dunite. Cations are based on four and fourteen oxygen for olivine and serpentine, respectively.

SUPPLEMENT FIGURE AND TABLE CAPTIONS

867 Fig. S1. Diagram showing lack of correlation between the IMF (‰) and $^{16}O^-$ secondary ion yields ($^{16}O^-$
868 cps / Primary beam intensity) in San Carlos olivine. The data can be retrieved from Table S2. The
869 $\alpha^{18}O_{SIMS}$ (Eq. 1) was converted in ‰-notation according to the following equation (e.g., Kita et al., 2009;
870 Śliwiński et al., 2016): IMF (‰) = $1000 \times 10\alpha^{18}O_{SIMS} - 1$).
871
872 Fig. S2. Diagram showing the extent of matrix bias measured by Scicchitano et al. (2018) in the lizardite
873 reference material L3431 and in the chrysotile reference material C22908 (section parallel to the
874 elongation axis) when referenced to antigorite Al06-44A, as a function of Mg#. Despite their similar
875 Mg/Fe ratio, a different matrix bias was observed relative to antigorite suggesting a potential effect of
876 crystal structure. Data can be retrieved from the online resources (Tables S1, S4 and S5) of Scicchitano
877 et al. (2018).
878
879 Table S1. SHRIMP oxygen isotope compositions (‰) of olivine reference materials referenced to San
880 Carlos olivine ($\delta^{18}O = 5.27 \pm 0.10$‰; Eiler et al., 1995; 2000; Bindeman et al., 2008; Ahn et al., 2012;
881 Isa et al., 2017).
882
883 Table S2. SHRIMP oxygen isotope compositions (‰) of San Carlos olivine used as a running standard
884 during analysis of the olivine reference materials.
885
886 Table S3. SHRIMP oxygen isotope compositions (‰) of olivine cores (Ol_C), olivine rims (Ol_R) and
887 lizardite (Lz) from the partly serpentinised dunite from the Nuasahi massif. Olivine and lizardite analyses
888 were referenced to San Carlos olivine ($\delta^{18}O = 5.27 \pm 0.10$‰; Eiler et al., 1995; 2000; Bindeman et al.,
889 2008; Ahn et al., 2012; Isa et al., 2017) and antigorite reference material Al06-44A ($\delta^{18}O = 8.30 \pm 0.12$‰;
890 Scicchitano et al., 2018), respectively.
891
892 Table S4. SHRIMP oxygen isotope compositions (‰) of San Carlos olivine and antigorite Al06-44A
893 used as running standards during analysis of the olivine and lizardite in the Nuasahi dunite.
894
895
896

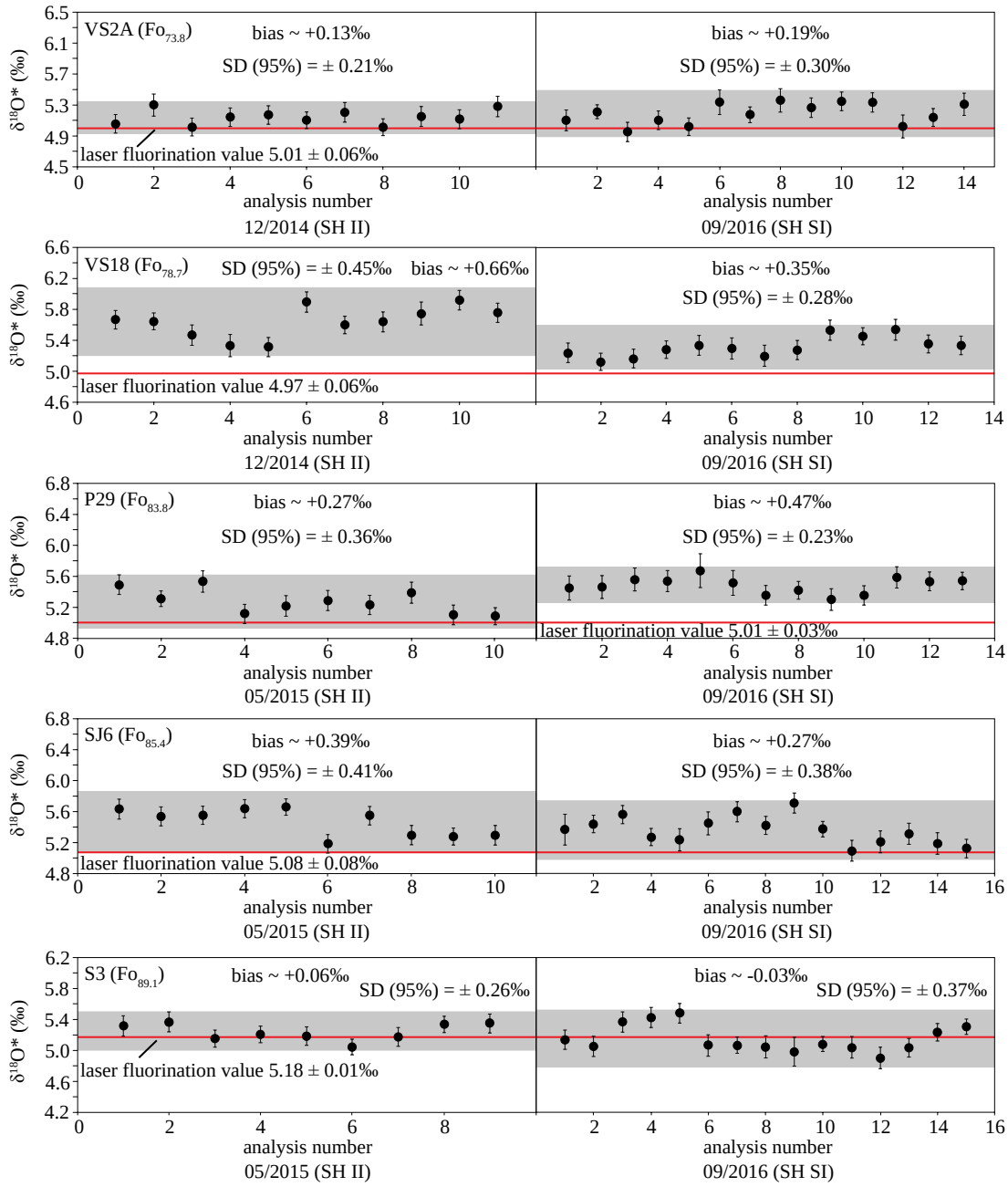
VS2A (Fo73.8)
bias ~ +0.13‰
SD (95%) = ± 0.21‰
laser fluorination value 5.01 ± 0.06‰
bias ~ +0.19‰
SD (95%) = ± 0.30‰
VS18 (Fo78.7)
SD (95%) = ± 0.45‰
bias ~ +0.66‰
laser fluorination value 4.97 ± 0.06‰
bias ~ +0.35‰
SD (95%) = ± 0.28‰
P29 (Fo83.8)
bias ~ +0.27‰
SD (95%) = ± 0.36‰
bias ~ +0.47‰
SD (95%) = ± 0.23‰
laser fluorination value 5.01 ± 0.03‰
SJ6 (Fo85.4)
bias ~ +0.39‰
SD (95%) = ± 0.41‰
laser fluorination value 5.08 ± 0.08‰
bias ~ +0.27‰
SD (95%) = ± 0.38‰
S3 (Fo89.1)
bias ~ +0.06‰
SD (95%) = ± 0.26‰
laser fluorination value 5.18 ± 0.01‰
bias ~ -0.03‰
SD (95%) = ± 0.37‰
δ18O* (‰)
analysis number
12/2014 (SH II)
09/2016 (SH SI)
05/2015 (SH II)

Fig. 1

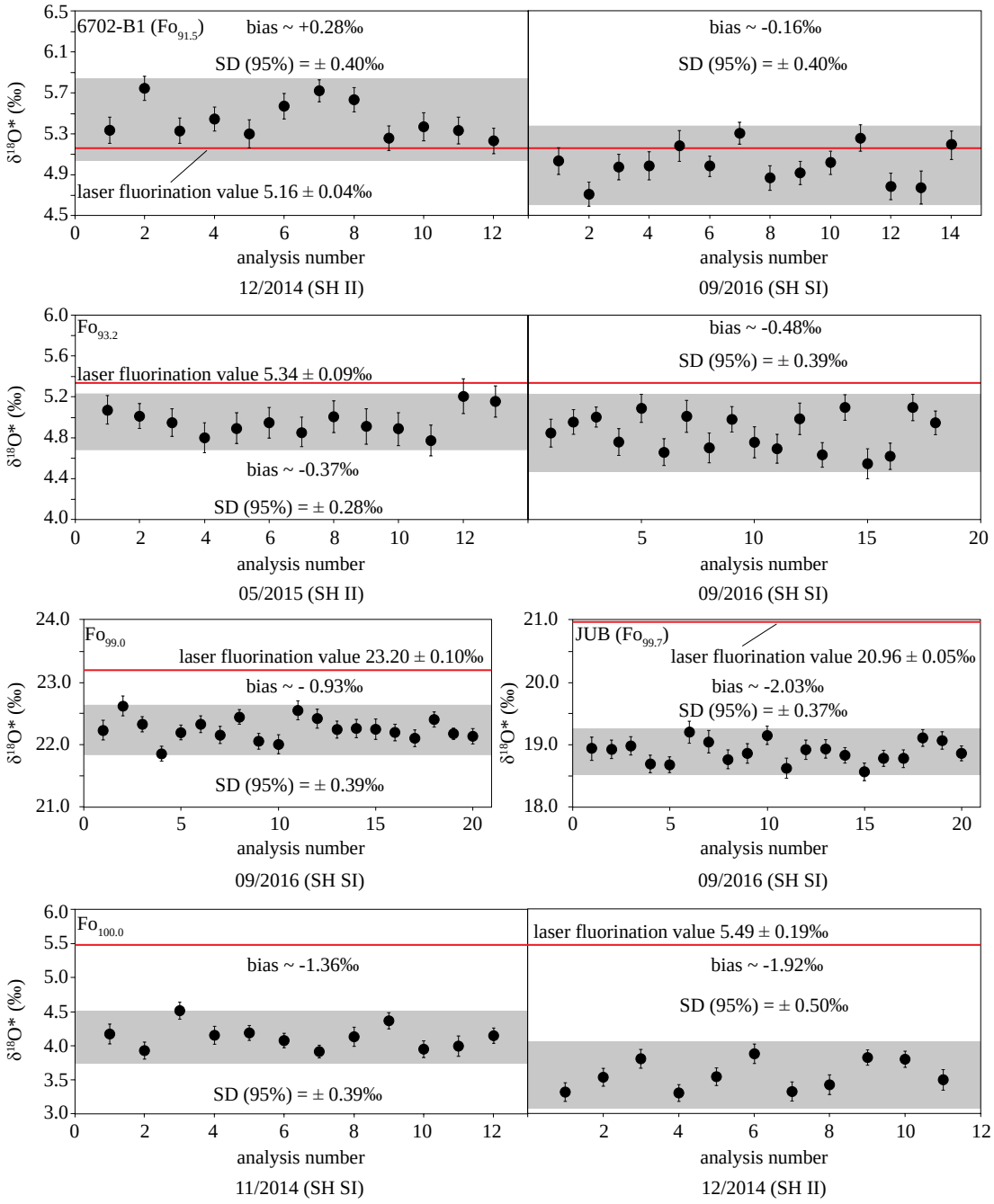

Fig. 1 (continued)

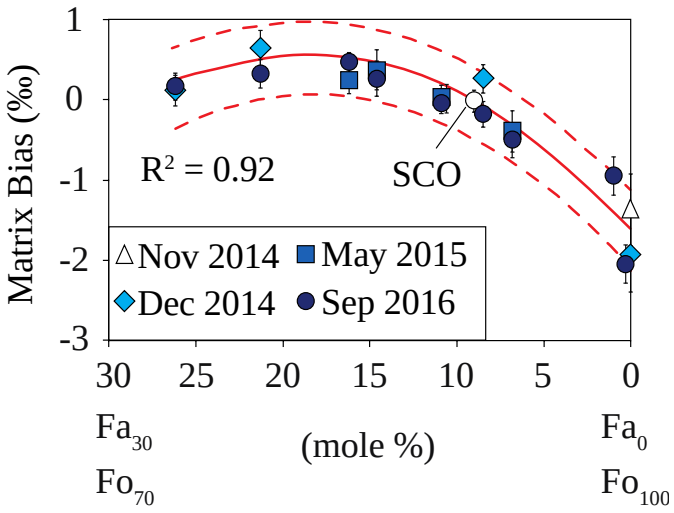
Matrix Bias (‰)
1
0
-1
-2
-3
R² = 0.92
SCO
Nov 2014
May 2015
Dec 2014
Sep 2016
30
25
20
15
10
5
0
Fa30
Fo70
(mole %)
Fa0
Fo100

Fig. 2

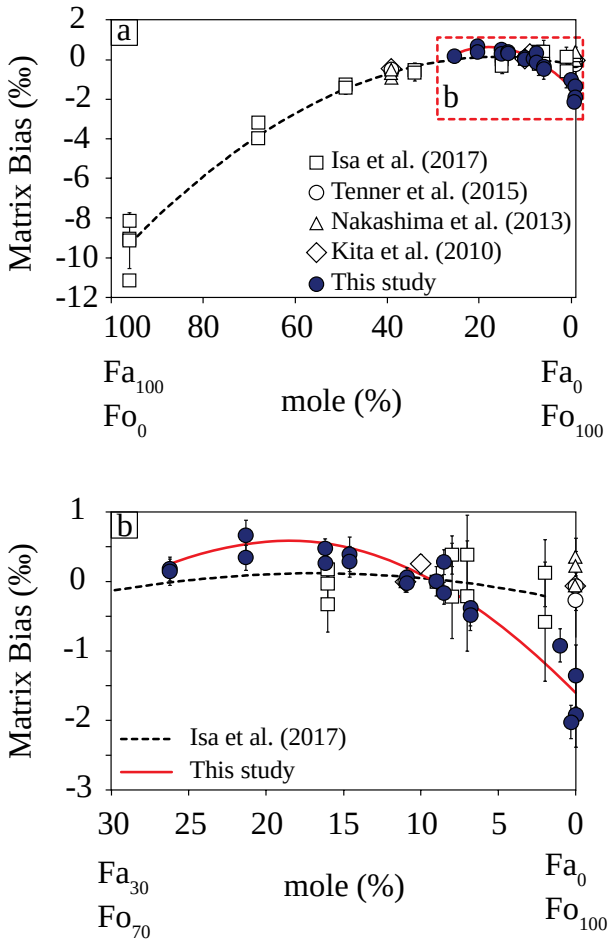
a
b
Matrix Bias (‰)
2
0
-2
-4
-6
-8
-10
-12
Isa et al. (2017)
Tenner et al. (2015)
Nakashima et al. (2013)
Kita et al. (2010)
This study
100
80
60
40
20
0
Fa100
Fo0
mole (%)
Fa0
Fo100
b
Matrix Bias (‰)
1
0
-1
-2
-3
Isa et al. (2017)
This study
30
25
20
15
10
5
0
Fa30
Fo70
mole (%)
Fa0
Fo100

Fig. 3

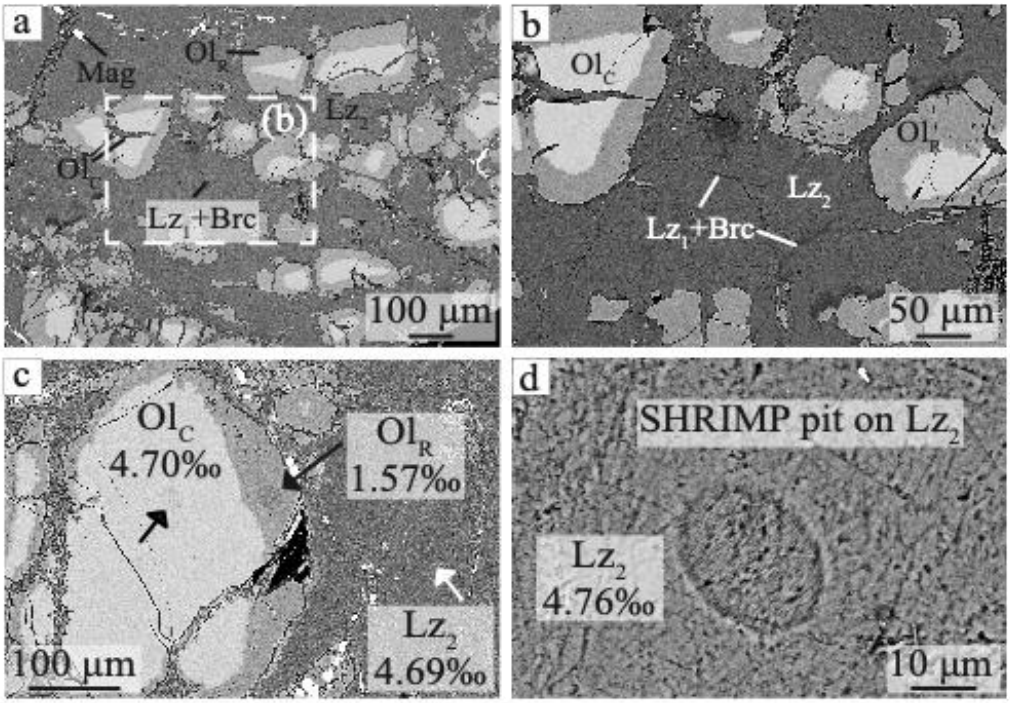
a
Mag
Ol
(b)
Lz
Ol
Lz1+Brc
100 µm
b
Olc
Olr
Lz2
Lz1+Brc
50 µm
c
Olc
4.70‰
Olr
1.57‰
Lz2
4.69‰
100 µm
d
SHRIMP pit on Lz2
Lz2
4.76‰
10 µm

Fig. 4

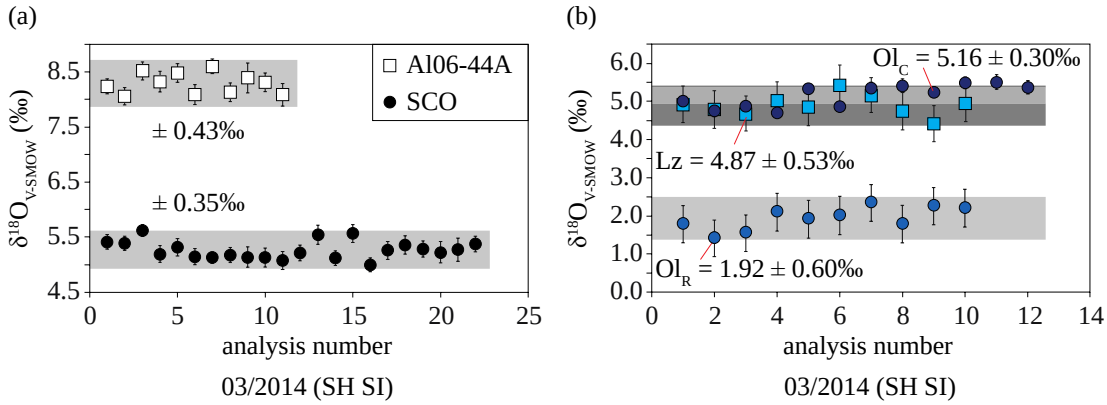
(a)
(b)
Al06-44A
SCO
± 0.43‰
± 0.35‰
δ18OV-SMOW (‰)
analysis number
03/2014 (SH SI)
OlC = 5.16 ± 0.30‰
Lz = 4.87 ± 0.53‰
OlR = 1.92 ± 0.60‰

Fig. 5

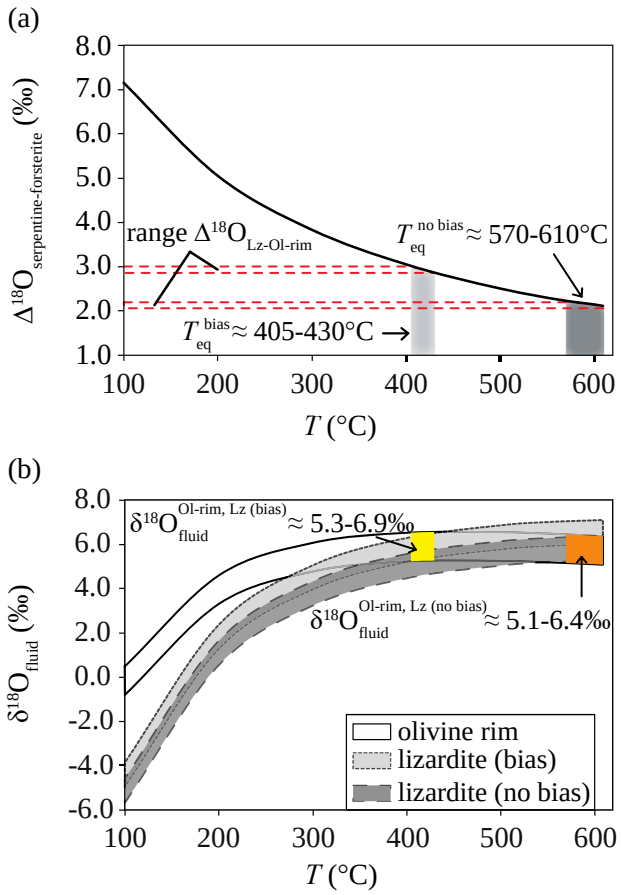
(a)
8.0
7.0
6.0
5.0
4.0
3.0
2.0
1.0
$\Delta^{18}O_{serpentine\text{-}forsterite}$ (‰)
range $\Delta^{18}O_{Lz\text{-}Ol\text{-}rim}$
$T_{eq}^{no\ bias} \approx$ 570-610°C
$T_{eq}^{bias} \approx$ 405-430°C →
100
200
300
400
500
600
T (°C)
(b)
8.0
6.0
4.0
2.0
0.0
-2.0
-4.0
-6.0
$\delta^{18}O_{fluid}$ (‰)
$\delta^{18}O_{fluid}^{Ol\text{-}rim,\ Lz\ (bias)} \approx$ 5.3-6.9‰
$\delta^{18}O_{fluid}^{Ol\text{-}rim,\ Lz\ (no\ bias)} \approx$ 5.1-6.4‰
olivine rim
lizardite (bias)
lizardite (no bias)
100
200
300
400
500
600
T (°C)

Fig. 6

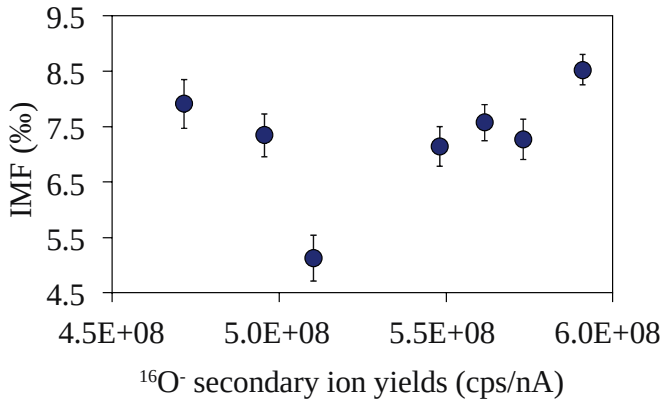
9.5
8.5
7.5
6.5
5.5
4.5
IMF (‰)
4.5E+08
5.0E+08
5.5E+08
6.0E+08
16O- secondary ion yields (cps/nA)

Fig. S1

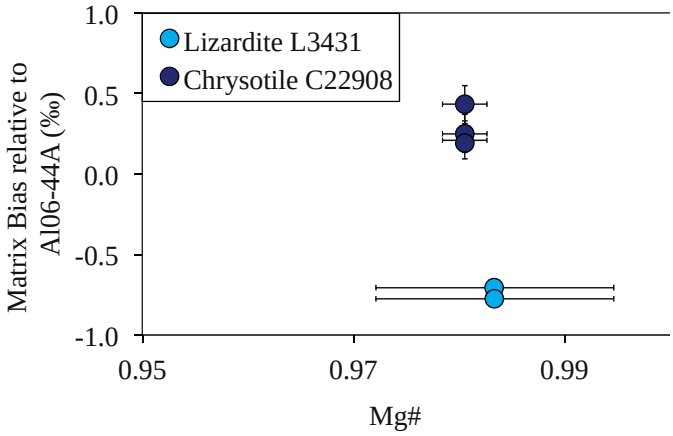

1035

1036 Fig. S2

Table 1

Sample	JUB*		Fo_{99}**		Fo_{93}**		Fo_{100}*		6702-B1*		VS2A**		VS18**		P29**		SJ6**		S3**	
Analysis	***n* = 11**	**1SD**	***n* = 3**	**1SD**	***n* = 3**	**1SD**	***n* = 13**	**1SD**	***n* = 10**	**1SD**	***n* = 3**	**1SD**	***n* = 3**	**1SD**	***n* = 6**	**1SD**	***n* = 6**	**1SD**	***n* = 6**	**1SD**
SiO_2	42,7	0,2	42,18	0,12	41,02	0,25	42,7	0,2	41,1	0,3	38,00	0,11	38,66	0,29	39,76	0,04	40,01	0,13	40,02	0,07
FeO_{total}	0,3	0,2	1,03	< 0.02	6,82	0,06	< 0.1	< 0.1	8,4	0,1	24,21	0,26	20,11	0,16	15,54	0,11	14,09	0,08	10,70	0,08
MnO	n.d.	-	0,02	< 0.02	0,10	< 0.02	n.d.	-	n.d.	-	0,49	0,02	0,37	< 0.02	0,24	< 0.02	0,20	< 0.02	0,15	< 0.02
MgO	57,3	0,2	57,51	0,17	52,85	0,15	57,5	0,2	50,3	0,3	38,22	0,13	41,67	0,14	45,09	0,15	46,16	0,27	48,99	0,14
CaO	n.d.	n.d.	0,03	< 0.02	< 0.02	< 0.02	n.d.	n.d.	n.d.	n.d.	0,15	< 0.02	0,15	< 0.02	0,25	< 0.02	0,27	< 0.02	0,29	< 0.02
NiO	< 0.1	< 0.1	< 0.02	< 0.02	0,39	0,02	< 0.1	< 0.1	0,5	< 0.1	0,02	0,02	0,08	0,02	0,19	0,02	0,21	0,02	0,29	0,02
Total	**100,4**	**0,4**	**100,78**	**0,05**	**101,18**	**0,30**	**100,2**	**0,3**	**100,2**	**0,4**	**101,10**	**0,24**	**101,04**	**0,27**	**101,06**	**0,11**	**100,94**	**0,29**	**100,44**	**0,26**
Si	1,00	< 0.01	0,99	< 0.01	0,98	< 0.01	1,00	< 0.01	1,00	< 0.01	0,99	< 0.01	0,99	< 0.01	0,99	< 0.01	0,99	< 0.01	0,98	< 0.01
Fe	0,01	< 0.01	0,02	< 0.01	0,14	< 0.01	0,00	-	0,17	< 0.01	0,53	0,01	0,43	0,01	0,32	< 0.01	0,29	< 0.01	0,22	< 0.01
Mn	n.d.	-	0,00	-	0,00	-	n.d.	-	n.d.	-	0,01	< 0.01	0,01	< 0.01	0,01	< 0.01	0,00	-	0,00	-
Mg	2,00	< 0.01	2,01	0,01	1,89	< 0.01	2,00	< 0.01	1,82	< 0.01	1,48	0,01	1,58	< 0.01	1,68	< 0.01	1,71	0,01	1,80	< 0.01
Ca	0,00	-	0,00	-	0,00	-	0,00	-	0,00	-	0,00	-	0,00	-	0,01	< 0.01	0,01	< 0.01	0,01	< 0.01
Ni	0,00	-	0,00	-	0,01	< 0.01	0,00	-	0,01	< 0.01	0,00	-	0,00	-	0,00	-	0,00	-	0,01	< 0.01
Sum of Cations	**3,01**	**< 0.01**	**3,02**	**< 0.01**	**3,02**	**< 0.01**	**3,00**	**< 0.01**	**3,00**	**< 0.01**	**3,01**	**< 0.01**	**3,01**	**< 0.01**	**3,01**	**< 0.01**	**3,00**	**< 0.01**	**3,02**	**< 0.01**
Fo (mole %)* **	**99,7**	**0,2**	**99,0**	**< 0.1**	**93,2**	**0,1**	**100,0**	**< 0.1**	**91,5**	**0,1**	**73,8**	**0,3**	**78,7**	**0,2**	**83,8**	**0,1**	**85,4**	**0,1**	**89,1**	**0,1**

* Analyses were performed with the Hitachi-4300 scanning electron microscope. ** Analyses were performed with the Jeol JXA-8200 electron microprobe. *** The forsterite content is calculated by considering total iron as ferrous iron. n.d. = not determined.

Table 2

Sample ID	Fo (mole %) (*)	Provenance (**)	$\delta^{18}O_{V\text{-}SMOW}$	1σ	*n*	Reference
Fo_{100}	100,0	Synthetic (Solix Corporation Belarus)	5,49	0,19	3	this study
Fo_{99}	99,0	Unknown	23,20	0,10	1	this study
Fo_{93}	93,2	Pakistan	5,34	0,09	2	this study
6702-B1	91,5	Lesser Antilles Islands (1)	5,16	0,04	3	P. Tollan (pers. comm.)
VS2A	73,8	Lesser Antilles Islands (2)	5,01	0,06	1	Tollan et al. (2012)
VS18	78,7		4,97	0,06	2	Tollan et al. (2012)
JUB	99,7	Ubehebe peak contact (3)	20,96	0,05	3	B. Putlitz (pers. comm.)
S3	89,1	Azores Islands (4)	5,18	0,01	1	Genske et al. (2013)
SJ6	85,4		5,08	0,08	1	Genske et al. (2013)
P29	83,8		5,01	0,03	1	Genske et al. (2013)

(*) Based on analyses performed in this study
(**) 1: Tollan et al. 2017; 2: Tollan et al. 2012; 3: Roselle et al. 1999; 4: Genske et al. 2013

Table 3

Mineral	Olivine core		Olivine rim		Lizardite$_2$	
Analysis	***n* = 2**	**1SD**	***n* = 3**	**1SD**	***n* = 8**	**1SD**
SiO_2	40,9	0,1	41,7	0,3	42,1	0,3
TiO_2	n. d.	-	n. d.	-	< 0.1	< 0.1
Al_2O_3	n. d.	-	n. d.	-	0,1	0,1
Cr_2O_3	n. d.	-	n. d.	-	0,1	0,1
FeO_{total}	7,5	0,1	1,8	0,2	3,5	0,4
MnO	< 0.1	< 0.1	< 0.1	< 0.1	< 0.1	< 0.1
MgO	51,4	0,2	56,3	0,1	41,0	0,3
CaO	< 0.1	< 0.1	< 0.1	< 0.1	< 0.1	< 0.1
NiO	0,2	0,2	0,2	0,3	0,2	< 0.1
H_2O calculated	-	-	-	-	12,8	0,1
Total	**100,0**	**< 0.1**	**100,0**	**< 0.1**	**99,7**	**0,1**
OH	-	-	-	-	8,0	-
Si	0,99	< 0.01	0,99	< 0.01	3,97	0,02
Ti	n. d.	-	n. d.	-	< 0.01	< 0.01
Al	n. d.	-	n. d.	-	0,01	0,01
Cr	n. d.	-	n. d.	-	0,01	0,01
Fe^{2+}	0,15	< 0.01	0,04	< 0.01	0,27	0,03
Mn	< 0.01	< 0.01	< 0.01	< 0.01	< 0.01	< 0.01
Mg	1,86	< 0.01	1,99	< 0.01	5,75	0,04
Ca	< 0.01	< 0.01	< 0.01	< 0.01	< 0.01	< 0.01
Ni	< 0.01	< 0.01	< 0.01	0,01	0,02	0,01
Sum of Cations	**3,01**	**< 0.01**	**3,01**	**0,01**	**10,02**	**0,02**
Mg# (mole %)	**92,4**	**0,1**	**98,2**	**0,2**	**95,5**	**0,5**